Published in final edited form as:
Basic Res Cardiol. 2008 November ; 103(6): 537–551. doi:10.1007/s00395-008-0740-1.

Effects of unipolar stimulation on voltage and calcium distributions in the isolated rabbit heart

Veniamin Y. Sidorov, Ph.D.[1,2,3], **Mark R. Holcomb, Ph.D.**[2], **Marcella C. Woods, Ph.D.**[1], **Richard A. Gray, Ph.D.**[1,3,5], and **John P. Wikswo, Ph.D.**[1,2,3,4]

[1]Department of Biomedical Engineering, Vanderbilt University, Nashville, Tennessee

[2]Department of Physics and Astronomy, Vanderbilt University, Nashville, Tennessee

[3]Vanderbilt Institute for Integrative Biosystems Research and Education, Vanderbilt University, Nashville, Tennessee

[4]Department of Molecular Physiology and Biophysics, Vanderbilt University, Nashville, Tennessee

[5]Department of Biomedical Engineering, University of Alabama, Birmingham, Alabama

Abstract

Background—The effect of electric stimulation on the polarization of cardiac tissue (virtual electrode effect) is well-known; the corresponding response of intracellular calcium concentration ($[Ca^{2+}]_i$) and its dependence on coupling interval between conditioning stimulus (S1) and test stimulus (S2) has yet to be elucidated.

Objective—Because uncovering the transmembrane potential (V_m) - $[Ca^{2+}]_i$ relationship during an electric shock is imperative for understanding arrhythmia induction and defibrillation, we aimed to study simultaneous V_m and $[Ca^{2+}]_i$ responses to strong unipolar stimulation.

Methods—We used a dual-camera optical system to image concurrently V_m and $[Ca^{2+}]_i$ responses to unipolar stimulation (20 ms, ±20 mA) in Langendorff-perfused rabbit hearts. RH-237 and Rhod-2 fluorescent dyes were used to measure V_m and $[Ca^{2+}]_i$, respectively. The S1-S2 interval ranged from 10 to 170 ms to examine stimulation during the action potential.

Results—The $[Ca^{2+}]_i$ deflections were less pronounced than changes in V_m for all S1-S2 intervals. For cathodal stimulation, $[Ca^{2+}]_i$ at the central virtual cathode region increased with prolongation of S1-S2 interval. For anodal stimulation, $[Ca^{2+}]_i$ at the central virtual anode area decreased with shortening of the S1-S2 interval. At very short S1-S2 intervals (10-20 ms), when S2 polarization was superimposed on the S1 action potential upstroke, the $[Ca^{2+}]_i$ distribution did not follow V_m and produced a more complex pattern. After S2 termination $[Ca^{2+}]_i$ exhibited three outcomes in a manner similar to V_m: non-propagating response, break stimulation, and make stimulation.

Conclusions—Changes in the $[Ca^{2+}]_i$ distribution correlate with the behavior of the V_m distribution for S1-S2 coupling intervals longer than 20 ms; at shorter intervals S2 creates more heterogeneous $[Ca^{2+}]_i$ distribution in comparison with V_m. Stimulation in diastole and at very short coupling intervals caused V_m - $[Ca^{2+}]_i$ uncoupling at the regions of positive polarization (virtual cathode).

Keywords

calcium dynamics; cardiac electrophysiology; membrane potential; optical mapping

Corresponding author: Dr. John P. Wikswo Department of Physics and Astronomy Vanderbilt University VU Station B 351807 Nashville, TN 37235-1807 Email: john.wikswo@vanderbilt.edu Tel: 615-343-4124 Fax: 615-322-4977.

Introduction

The intracellular calcium concentration ($[Ca^{2+}]_i$) plays a central role in the process of excitation-contraction coupling [33]. The behavior of $[Ca^{2+}]_i$ is tightly coupled with transmembrane potential (V_m) dynamics and is governed by sarcolemmal Ca^{2+} fluxes and by Ca^{2+}-transporting systems of the sarcoplasmic reticulum (SR) and mitochondria [4,42]. In normal conditions the activation of Ca^{2+} release from the SR is controlled by means of the Ca^{2+}-induced Ca^{2+} release mechanism mediated by sarcolemmal Ca^{2+} channels [5].

Alteration of the normal V_m - $[Ca^{2+}]_i$ relationship can underlie ectopic arrhythmias, such as those occurring during delayed afterdepolarizations [61] when SR Ca^{2+} overload promotes release of Ca^{2+} from the SR and activation of $[Ca^{2+}]_i$-dependent currents, resulting in the generation of an action potential (AP) [51]. Because V_m - $[Ca^{2+}]$ cycling is coupled bidirectionally [50] their relationship becomes more complex during ventricular tachycardia (VT) [12] and especially during ventricular fibrillation (VF) when Ca^{2+} waves could either precede or follow membrane depolarization [46]. However, the primary role of the V_m - $[Ca^{2+}]_i$ dissociation with respect to wave fragmentation remains controversial [64].

Since there is strong coupling between V_m and $[Ca^{2+}]_i$, it is reasonable to expect involvement of $[Ca^{2+}]_i$ in the process of defibrillation. Recently Hwang *et al.* observed that shock-induced high $[Ca^{2+}]_i$ heterogeneity is followed by an unsuccessful defibrillation shock and the regions of lower $[Ca^{2+}]_i$ were associated with first postshock activation [30]. On the single cell level the effect of electric field stimulation on the calcium transients (CT) was investigated by Sharma and Tung who showed uniform field-mediated polarization of the cell membrane can produce spatial heterogeneity of $[Ca^{2+}]_i$ in isolated guinea pig cardiomyocytes [54]. Elegant studies of V_m - $[Ca^{2+}]_i$ relationship during field shock were conducted in Vladimir Fast's laboratory [20,48]. The authors demonstrated shock-induced reduction of $[Ca^{2+}]_i$ in both the positively and negatively polarized sides of cultured cell strips obtained from neonatal rat myocytes [20]. They showed that current through the L-type voltage-dependent Ca^{2+} channels (I_{CaL}) may play an important role in the decrease of $[Ca^{2+}]_i$. In spite of the important contribution of this work it should be noted that developmental differences between neonatal and maturated cardiomyocytes, including T-tubular and SR structures [44,45], ryanodine receptor sensitivity [13,65], and variation in sarcolemmal Ca^{2+} channel activity [18,23,27, 60], could modify the Ca^{2+} response to electric shock in these two types of cells.

It is known that electric field stimulation of cardiac tissue occurs via virtual electrode mechanisms and that bidomain properties play a key role in this process [52,53]. Unipolar stimulation creates a polarization pattern consisting of a central dog-bone shaped area with the polarity of the stimulus flanked by two virtual electrode regions of opposite polarity [37,43, 66]. In our work we utilized unipolar electrical stimulation of the isolated rabbit heart to produce predictable virtual electrode polarization patterns and investigate systematically, for the first time, the spatio-temporal distributions of $[Ca^{2+}]_i$ and the V_m - $[Ca^{2+}]_i$ relationship through the cardiac cycle as well as test the hypothesis that the V_m - $[Ca^{2+}]_i$ relationship during electrical stimulation of adult cardiac cells in the whole heart preparation differs from the V_m - $[Ca^{2+}]_i$ relationship in a monolayer of neonatal cardiomyocytes in a culture dish due to developmental and anatomical differences.

Methods

Experimental Preparation

All experiments were conducted in accordance with the National Institutes of Health regulations for the ethical use of animals in research and were approved in advance by the Vanderbilt Institutional Animal Care and Use Committee.

New Zealand white rabbits (N = 7) of either sex weighing 2.7 to 3.1 kg were used in the experiments. The detailed description of the heart preparation has been published previously [56]. The animals were preanesthetized with ketamine (50 mg/kg), heparinized (1,000 units) and anesthetized with sodium pentobarbital (60 mg/kg). The heart was quickly removed from the chest and mounted on a Langendorff apparatus for retrograde perfusion with oxygenated Tyrode's solution of the following composition (mM): 133 NaCl, 4 KCl, 2 $CaCl_2$, 1 $MgCl_2$, 1.5 NaH_2PO_4, 20 $NaHCO_3$, and 10 glucose. The excitation-contraction uncoupler 2,3-butanedione monoxime (BDM [Sigma-Aldrich, St. Louis, MO]) was added to the perfusate (15 mM) to eliminate contractile optical artifacts. The hearts were exposed to air during the experiments. To stain the heart with the calcium-sensitive dye Rhod-2AM [11,46,49], 1 mL of the dye stock solution (0.5 mg/mL DMSO) was slowly delivered via an injection port above the aorta. Thereafter 10 μL of the voltage-sensitive dye RH-237 (1 mg/mL DMSO) was gradually administered through the same injection port.

To examine the potential effect of BDM on the calcium response, an additional series of experiments (N = 3) with blebbistatin (Sigma-Aldrich, St. Louis, MO) as the excitation-contraction uncoupler [16,21] were conducted. Stock solution of blebbistatin (2.5 mg/mL DMSO) was added to the perfusate to obtain a concentration of 3 μM. In these experiments the hearts were stained only with the calcium-sensitive dye Rhod-2AM.

Optical System

For the hearts stained with both RH-237 and Rhod-2AM a dual-camera system was used [28]. Each DALSA CCD camera (DS-12-16K5H, 128×128 pixels, 490 fps, Dalsa Inc., Waterloo, ON, Canada) is supported by a custom mount on a tilt rotation stage (Newport P080N, Irvine, CA), which allows quick and accurate mechanical alignment of the cameras. The base plate accommodates the cameras horizontally and allows various combinations of lenses and working distances. A dichroic mirror is situated at 45 degrees with respect to both cameras and reflects the $[Ca^{2+}]$ signal (< 635 nm) and transmits the V_m signal (>635 nm). The V_m camera uses a 710 nm long pass filter (710AELP, Omega Optical), and the $[Ca^{2+}]$ camera uses a 585 ± 20 nm band pass filter (585AF40, Omega Optical). Both cameras have a lens (25 mm 1” format C-mount, Navitar) to which the filters are attached by a custom connector. The magnification was adjusted to focus on a 15 × 15 mm^2 area. Two Bitflow R3 frame grabbers (Bitflow, Boston, MA) and a timer board (National Instruments PCI 6602) are installed in a Dell 650 Pentium IV/3 GHz Precision Workstation to synchronize the cameras and control stimulation. Custom-developed “C”-based software controls data acquisition, camera synchronization, external stimulation and laser illumination. The fluorescence is excited by diode-pumped, solid-state laser (Verdi, Coherent, Santa Clara, CA) at a wavelength of 532 nm.

In the blebbistatin experiments in which only Rhod-2AM was used, a single high-speed, lower-noise RedShirt CCD camera (14-bit, 80×80 pixels, 1000 fps, CardioCCD-SMQ, RedShirt Imaging) was utilized to image $[Ca^{2+}]_i$ over 8 × 8 mm^2. The band pass filter (585AF40, Omega Optical) and lens (25 mm 1″ format C-mount, Navitar) were the same as in DALSA dual-camera setup.

Stimulation Protocol

The anterior left ventricle was mapped. The heart was continuously paced (2 ms duration, 2× diastolic threshold) at a cycle length of 300 ms via a bipolar platinum electrode [56] placed on the right ventricle close to the septum, 8–9 mm from the unipolar testing electrode. The unipolar testing electrode (delivering the S1 conditioning stimuli and S2 test stimuli), also made from platinum wire (0.25-mm diameter), was positioned on the anterior left ventricle, and the cameras' fields of view were centered with respect to the testing electrode. For the S1 conditioning stimuli (2-ms duration), the current strength was set slightly above diastolic threshold and the interval between S1 and the previous pacing stimulus was 300 ms. Three sequential S1 stimuli were applied prior to the delivery of the S2 premature test stimulus of either negative or positive polarity. The duration and amplitude of S2 were 20 ms and 20 mA, respectively. The S1-S2 coupling intervals were progressively shortened beginning at 190 ms in 20-ms steps down to 50 ms and after that in 10-ms steps down to the shortest S1-S2 interval tested, 10 ms. A piece of titanium mesh against the posterior LV served as the reference electrode for the S1 and S2 stimuli.

Spectral Overlap Estimation

To estimate the spectral overlap between RH-237 and Rhod-2AM fluorescence, an additional six hearts underwent two separate experimental protocols. In the first protocol (3 hearts), at the beginning of the experiment the heart was stained only with the V_m-sensitive dye RH-237 and both voltage and “calcium” images were recorded using the respective filters. The data acquired through the calcium filter represented the bleed-through of the voltage signal, which we termed the calcium error (error $[Ca^{2+}]_i$). Thereafter the Ca^{2+}-sensitive dye Rhod-2AM was administered, and data were acquired while the heart was continuously stimulated at a pacing rate of 300 ms. In the second experimental protocol (3 hearts), only Rhod-2AM was used at first. In this situation, the “voltage” images represented the voltage error (error V_m). After collecting data, the heart was then stained with RH-237, the pacing protocol was repeated, and voltage and calcium fluorescence were recorded again. To calculate the error due to overlap of the voltage and calcium spectra, the amplitude of the calcium transient error was normalized to the amplitude of $[Ca^{2+}]_i$:

$$\%\ \text{error}\left[Ca^{2+}\right]_i = \left(\text{error}\left[Ca^{2+}\right]_i / \left[Ca^{2+}\right]_i\right) \times 100\%.$$

The error for voltage measurements was calculated as the amplitude of the voltage error normalized to the amplitude of the V_m signal:

$$\%\ \text{error}\ V_m = (\text{error}\ V_m / V_m) \times 100\%.$$

Spectral Recording

A miniature fiber optic spectrometer (USB2000, Ocean Optics, FL, USA) was used to record the fluorescence spectra of RH-237 and Rhod-2AM from 200 to 1100 nm. The spectrometer comprises optical elements coupled with 2048-element linear silicon CCD array detector which is responsive from 200 to 1100 nm.

Data Processing and Statistical Analysis

The optical data collected with the Dalsa dual-camera system were first processed by an 8 × 8 Gaussian spatial filter and a 3-point mean temporal filter. The data acquired with RedShirt camera were filtered only using a 5 × 5 Gaussian spatial filter. Thereafter the $[Ca^{2+}]_i$ and V_m data were normalized pixel-by-pixel according to fluorescence changes during the last pacing

response and are presented as the percentage of this AP amplitude. To demonstrate the net effect of S2 stimulation on V_m and $[Ca^{2+}]_i$ distributions, the previous S1 response was subtracted from the S2 response for some analyses. We will refer to these potential and intracellular calcium distributions as ΔV_m and $\Delta[Ca^{2+}]_i$ accordingly. The conduction velocity was computed using the time-space plot method [56]. To construct the temporal derivative maps, the data were additionally preprocessed with a 5×5 spatial and 5-point mean temporal filters.

Six rabbit hearts were studied to estimate the optical overlap between calcium and voltage fluorescence; seven rabbit hearts were used to examine the effects of cathodal and anodal stimulation; and three rabbit hearts were utilized to estimate the effects of BDM on $[Ca^{2+}]_i$ dynamics. Group data are presented as mean ± standard deviation. Statistical analysis was performed utilizing the paired *t*-test. Differences were considered significant when $P < 0.05$.

Results

Emission spectra and estimation of spectral overlap

Figure 1A illustrates the emission spectra of Rhod-2AM and RH-237 measured separately in two different experiments. Based on these measurements, a band pass filter (585 ± 20 nm) and a long pass filter (> 710 nm) were chosen to minimize spectral overlap without significantly sacrificing signal intensity. Figure 1B and 2C demonstrate the fluorescence recordings when hearts were stained with either RH-237 or Rhod-2AM, respectively. No prominent RH-237 fluorescence bleeding through the band pass filter is observed in Fig 1B (lower trace). The mean % error of $[Ca^{2+}]_i$ was 3.97 ± 1.66 (3 hearts). If the heart was stained only with Rhod-2AM (Fig. 1C), slight leakage of $[Ca^{2+}]_i$ fluorescence through the long pass filter is observed (lower trace). The mean % error of V_m was 4.45 ± 1.94 (3 hearts).

Changes in V_m and $[Ca^{2+}]_i$ during the shock

Figure 2 shows the voltage and calcium responses during stimulation of –20 mA amplitude and 20 ms duration at different S1-S2 coupling intervals. Panel A demonstrates the maps of V_m and $[Ca^{2+}]_i$ distribution at the end of S2. Net V_m and $[Ca^{2+}]_i$ changes after subtraction of the previous S1 response (ΔV_m and $\Delta[Ca^{2+}]_i$) are illustrated in panel B. The characteristic virtual electrode polarization pattern [66] for cathodal stimulation is observed in the V_m images: a dogbone-shaped region of positive polarization (virtual cathode, VC) oriented transverse to the fiber direction with flanking regions of negative polarization (virtual anodes, VA) aligned parallel to the fiber direction. Traces from the VC (white dot) and VA (blue dot) regions superimposed with traces recorded at the same locations from the previous S1 wave (black) are shown in panels C and D, respectively.

The magnitudes of ΔV_m are larger than the magnitudes of $\Delta[Ca^{2+}]_i$ over the full range of tested S1-S2 intervals. The maps of V_m and ΔV_m distribution (panels A and B) reveal nonlinear behavior: the magnitude of VA hyperpolarization decreases with prolongation of the S1-S2 interval whereas VC depolarization becomes more prominent [2,9,19,25]. For coupling intervals of 30 ms or longer, the distribution of $\Delta[Ca^{2+}]_i$ correlates with the distribution of ΔV_m. When S2 is delivered very soon after S1 (S1-S2 coupling interval of 10 ms), two blue areas oriented transverse to the fiber direction on opposite sides of the central electrode appear in the $\Delta[Ca^{2+}]_i$ map in Fig. 2B; these areas indicate delayed $[Ca^{2+}]_i$. The V_m and $[Ca^{2+}]_i$ traces for the VC pixel located within these areas (white dot in top of panel A) show that S2 increases the slope of the AP upstroke, but decreases the slope of CT upstroke (Fig. 2C, top row). In the VA region (blue dot in top of panel A), both voltage and calcium optical signals decrease during S2 (Fig. 2D, top row). When the S1-S2 interval was increased to 20 ms, the blue areas located centrally the in $\Delta[Ca^{2+}]_i$ image (panel B, S1-S2 interval of 10 ms) moved away from the center

transversely to the fiber direction such that four blue regions are clearly observed (panel B, S1-S2 interval of 20 ms). This four-petalled pattern of negative $\Delta[Ca^{2+}]_i$ deflection was detected in all seven experiments.

Figure 3 illustrates the voltage and calcium responses during stimulation of the opposite polarity (anodal). S2 amplitude (20 mA) and duration (20 ms) as well as S1-S2 coupling intervals are the same as in Figure 2. The central VA area reveals a strongly negative $\Delta[Ca^{2+}]_i$ for the 10-ms coupling interval (Fig. 3B): the delays in AP and CT upstrokes are clearly seen in top row in Figure 3D. When the S1-S2 interval is lengthened to 20 ms, the VA-related negative $\Delta[Ca^{2+}]_i$ becomes weaker and the only easily visible region of strong negative change in $[Ca^{2+}]_i$ occurs at the upper right edge of the VA (Fig. 3B). The four-petalled pattern, which was detected during negative S2 stimulation as shown in Figure 2B, was not as pronounced for this polarity. The central blue area of negative $\Delta[Ca^{2+}]_i$ correlates with the region of negative V_m (the VA) in all seven experiments, becoming less prominent with S1-S2 prolongation. The areas of elevated $\Delta[Ca^{2+}]_i$ corresponding to the VCs become evident only for coupling intervals 70 ms and longer.

Figures 4 A and B demonstrate the mean values of net ΔV_m and $\Delta[Ca^{2+}]_i$ near the stimulating electrode during cathodal (grey) and anodal (black) S2 as a function of coupling interval. The intersection of the black curves and the zero lines in panels A and B correspond to the transition of stimulation mechanism from break to make. Figure 4 C includes all measurements acquired in seven experiments; here, the differences in the magnitude of $\Delta[Ca^{2+}]_i$ resulting from changes in S2 polarity and in coupling interval are shown to correlate well with those for V_m.

Figure 5 shows the calcium response when blebbistatin was applied as an excitation-contraction uncoupler. As in the experiments with BDM, stimuli of 20 mA magnitude and 20 ms duration of both polarities were tested. At the 10-ms coupling interval, two dark blue areas indicate delay in CT upstroke during both cathodal and anodal stimulations (Fig. 5A). Beginning with the S1-S2 interval of 30 ms the VA-associated decrease in $[Ca^{2+}]_i$ is evident during both cathodal and anodal stimulations. The increase of $[Ca^{2+}]_i$ related with the VC becomes prominent at the 110-ms coupling interval.

Postshock V_m and $[Ca^{2+}]_i$ activity

Typical outcomes from cathodal and anodal stimulation are represented in Figures 6 and 7, respectively. These data were obtained in a separate experiment from those shown in Figures 2 and 3. V_m and $[Ca^{2+}]_i$ dynamics are illustrated in terms of derivatives of optical signals.

Figure 6A represents the situation when the S1-S2 interval of 90 ms was too short to allow global propagation, such that charge diffusion after cathodal S2 termination (20 ms) induces only local V_m arising in the VAs but not a propagating AP. The images of $d[Ca^{2+}]_i/dt$ do not reveal detectable elevation of $[Ca^{2+}]_i$ at the VC during the 20-ms stimulus. After S2 termination, the increasing V_m in the VAs causes prominent changes in $[Ca^{2+}]_i$ (Fig. 6A, 30 and 40 ms). Figure 6B demonstrates break stimulation at the S1-S2 interval of 150 ms. The increasing $[Ca^{2+}]_i$ in the VC becomes noticeable in the 10 and 20-ms frames. After cessation of S2, charge diffusion initiates excitation at the VAs. In the time interval between 30 and 70 ms, the S2-induced V_m wave revolves around four sites marked with four green dots (Fig. 6B, 40 ms) and invades the central VC region. Due to depressed excitability at the VC, the wave front decays and disappears, completing one cycle of quatrefoil reentry. $[Ca^{2+}]_i$ exhibits the same dynamics, but with delay. Figure 6C illustrates V_m and $[Ca^{2+}]_i$ dynamics during stimulation in diastole using a coupling interval of 300 ms. Excitation occurs before S2 termination. Two dark VA regions in the 10-ms image of dV_m/dt indicate delay in excitation caused by negative polarization. After S2 termination the rising V_m at the VAs produces a two-petalled pattern in the 30-ms dV_m/dt image. The behavior of $[Ca^{2+}]_i$ is different. In addition

to the delay in the VAs, the central VC region also exhibits lagging $[Ca^{2+}]_i$ response (10-ms image of $d[Ca^{2+}]_i/dt$). As a result the S2 cessation promotes increasing $[Ca^{2+}]_i$ in the VAs and VC areas, thereby causing a four-petalled pattern that is clearly seen in the 30 and 40-ms images.

The conduction velocities for V_m propagation in diastolic tissue along (CV_L) and transverse (CV_T) to the fiber direction were 61.57 ± 4.02 cm/s and 22.09 ± 3.24 cm/s, respectively (N = 7). These values for $[Ca^{2+}]_i$ statistically differed from V_m ($P < 0.05$) and comprised 55.86 ± 4.68 cm/s and 18.94 ± 3.61 cm/s (N = 7). The mean value of the CV_L/ CV_T ratio for $[Ca^{2+}]_i$ propagation (3.01 ± 0.43) was higher than that for V_m propagation (2.82 ± 0.31) ($P < 0.05$). To investigate if pacing rate influences the difference between CVs for V_m and $[Ca^{2+}]_i$ propagation, three additional experiments were conducted (not shown). In these experiments the hearts were stimulated transverse and along the fiber direction at different pacing rates. Progressively decreasing the pacing interval from 300 ms down to 140 ms did not produce any substantial effect on the CV disparity for steadily propagating V_m and $[Ca^{2+}]_i$ waves.

Figure 7 shows the outcomes for anodal S2 stimulation. Three cases, no propagating response (Fig. 7A), break stimulation (Fig. 7B), and make stimulation (Fig. 7C), were created with S1-S2 intervals of 90, 150, and 300 ms, respectively. In Figure 7A the elevation of $[Ca^{2+}]_i$ during stimulation is too slow to be detected with the derivative (10 and 20-ms images). After S2 termination, charge spreads from the VCs into the central VA area resulting in elevation of V_m and $[Ca^{2+}]_i$ (Fig. 7A, 30-ms image). The 40-ms images reveal decay of the local V_m and $[Ca^{2+}]_i$ responses. When the coupling interval is increased to 150 ms (Fig. 7B), after S2 cessation charge diffusion from the VCs was sufficient to initiate a propagating wave at the central VA region (20 and 30-ms images). During propagation the wave fronts become convex and turn around four sites (Fig. 7B, 40 ms). Because the VCs have not sufficiently recovered, after collision the waves do not enter the VCs to complete one full cycle of reentry but, instead, form a common ellipsoid wave front propagating outwardly (Fig. 7B, 50 ms). Stimulation in diastole causes fast elevation of V_m at the VCs (Fig. 7C, 10 ms). The central dark regions located transversely to the fiber direction indicate delayed V_m elevation at the VA area during S2, which then exhibit increasing V_m after S2 termination (30 ms). The images of $d[Ca^{2+}]_i/dt$ show deceleration of $[Ca^{2+}]_i$ response in both central VA and flanked VCs regions during S2 (10 ms). After S2 cessation the delayed $[Ca^{2+}]_i$ increase at the VA and VCs results in a four-petal pattern in the 30 and 40-ms images. Note that although cathodal and anodal stimulation produce reversed patterns of dV_m/dt distribution during stimulation in diastole, the $d[Ca^{2+}]_i/dt$ images after S2 termination reveal similar patterns for both polarities (Fig. 6C and Fig. 7C).

Another of our observations was prolongation of CT at regions of both positive and negative polarization (Fig. 2C, D and Fig. 3C, D). The largest increase in CT duration, measured at the 50% level of recovery, was 27.4 ± 6.5 % (7 hearts) for cathodal stimulation and 31.5 ± 10 % (7 hearts) when S2 was anodal.

Discussion

In this study we show that for coupling intervals longer than 20 ms the changes in the $[Ca^{2+}]_i$ distribution resemble the behavior of V_m distribution for both negative and positive stimulation. However $[Ca^{2+}]_i$ fractional changes are smaller than those changes in V_m. The average $\Delta V_m/\Delta[Ca^{2+}]_i$ ratio in the central virtual electrode for coupling intervals of 30 – 130 ms is 4.52 ± 1.39 and 4.54 ± 0.49 (N = 49: 7 hearts for 7 tested coupling intervals) for cathodal and anodal S2, respectively. When stimulation is cathodal, $[Ca^{2+}]_i$ at the central VC region increases with prolongation of the S1-S2 interval. If stimulation is anodal, $[Ca^{2+}]_i$ at the central VA area decreases with shortening of the S1-S2 interval. For very short coupling intervals (10-20 ms), the S1 wave front only begins to spread before S2 is applied. Therefore S2 is

applied while the tissue exhibits greatly different stages of excitation: V_m around the electrode is in the upstroke phase, while tissue outside of the elliptical S1 wave front is at rest. In this case the largest V_m and $[Ca^{2+}]_i$ gradients exist at the vicinity of stimulation location. As a result the $\Delta[Ca^{2+}]_i$ distribution exhibits patterns dissimilar to ΔV_m. The distinction is more evident for cathodal stimulation when mismatch exists between ΔV_m elevation and $\Delta[Ca^{2+}]_i$ reduction at the central VC area. During anodal stimulation the S2 hyperpolarization delays excitation causing negative $\Delta[Ca^{2+}]_i$ (Fig. 3B 10-ms S1-S2 interval).

It was demonstrated recently that uniform field stimulation at the beginning of plateau phase can induce declining $[Ca^{2+}]_i$ at both the negatively and positively polarized sides in neonatal rat cell culture strands [20,48]. Nifedipine eliminated the shock-induced decrease in $[Ca^{2+}]_i$ at the depolarized side of the cell culture strand, indicating the main role of I_{CaL} in this effect. It was suggested that when V_m exceeds reversal potential for I_{CaL}, the current changes direction from inward to outward and, consequently, could be responsible for $[Ca^{2+}]_i$ reduction at the cathodal end of the cell culture preparation. The hyperpolarization at the opposite side of the strand can also cause a decline of $[Ca^{2+}]_i$ because of inactivation of the L-type Ca^{2+} channels, Ca^{2+} efflux via Na^+/Ca^{2+} exchangers (NCX), and binding with troponin [20,48].

In our experiments we did not detect decreasing $[Ca^{2+}]_i$ at the VC during stimulation early in the plateau at 30 and 40-ms S1-S2, while the negative changes of $[Ca^{2+}]_i$ at the VA areas (~ 12 %) were comparable to those observed by Fast *et al.* in neonatal rat cardiomyocyte cultures (~ 15 %) [20,48]. Furthermore, as we have mentioned above, VC depolarization caused elevation of $[Ca^{2+}]_i$ with increasing S1-S2 interval. In the range of coupling intervals between 30 ms and 130 ms, the values of $\Delta[Ca^{2+}]_i$ due to cathodal S2 had a minimum of 3.1% and maximum of 16.6%. Those values due to anodal S2 were -12.6% and -6.4%, respectively (Fig. 4B). These results are qualitatively in agreement with those detected with S1-S2 prolongation in strands of cultured cardiomyocytes [48]. The discrepancy in $[Ca^{2+}]_i$ behavior observed in the VC region is probably due to either one or both of the following reasons: (1) inadequate depolarization magnitude to cause reversal of I_{CaL} and (2) the distinction in $[Ca^{2+}]_i$ handling due to species-dependent and developmental disparities between neonatal and mature cells.

The magnitudes of polarization observed in our preparations were weaker than those reported in cultured myocytes [8]. The maximum ΔV_m values during stimulation at the beginning of AP plateau for S1-S2 coupling intervals between 30 and 50 ms were 28% and 46% for positive and negative deflections, respectively. These values in cell culture preparations were about 60% and 200% for cathodal and anodal polarizations [8,20]. Such substantial disparity could be result of differing stimulation modes. Point stimulation on the surface of the heart produces polarization that decays exponentially with depth at a distance comparable to the length constant [31]. The value of length constant depends on the cardiac cell type and the fiber direction. The length constant is typically less than 1 mm [35,36] and is shorter transverse to the fiber direction [38]. In addition, the length constant is also affected by anatomical structure due to differences in electrotonic coupling. Because current spreads multi-dimensionally, the electrotonic voltage decrement in a three-dimensional preparation would be steeper with distance causing the length constant to be shorter than in one- or two- dimensional preparations.

In addition, bidomain effects visible in the intact myocardium can be severely attenuated in a confluent layer of cardiomyocytes at the bottom of a culture dish. In culture, the depth of the culture media may be one hundred to one thousand times the thickness of the cell layer. In myocardium, the extracellular space may account for less than 20 % of the tissue volume. Hence the effect of extracellular resistivity, anisotropy and current distributions may be quite different between the two preparations.

Optical signals measured from the heart surface are weighted averages of fluorescence from a tissue depth [24,31] estimated to be between 0.3 – 0.5 mm [22,37] and 1 – 2 mm [3,7,15,17]. If the optical decay constant is greater than the electrical length constant, the optical signals arising from the deeper layers, unaffected by the stimulus, can cause underestimation of the surface ΔV_m. In monolayer cell cultures the optical signals are not attenuated by averaging over depth and therefore exhibit larger deflections.

It is known that excitation-contraction coupling undergoes extensive transformations during postnatal development [27,57,63]. In contrast with adult cardiomyocytes, neonatal cells have underdeveloped SR [45], so the significant fraction of activator Ca^{2+} enters through the sarcolemmal Ca^{2+} transportation system [62]. Among the most essential electrophysiological properties of neonatal cells which could modify the $[Ca^{2+}]_i$ response of cell cultures to electric shock are longer AP [27,63], increased sarcolemmal Ca^{2+} current [23,27], and lower sensitivity to ryanodine [13]. Besides developmental changes, the cell culture procedure itself can promote cellular remodeling, affect the excitation-contraction coupling and, consequently, could alter the response to electrical stimulation. In particular, Snopko *et al.* recently reported that sarcolemmal Ca^{2+} entry is enhanced at least two-fold in rat cardiomyocytes at the fourth day of culturing in comparison to acutely dissociated cardiomyocytes from new born rat hearts of the equivalent age [57].

The unexpected finding of our study was the counter effect of strong negative stimulation on the upstroke dynamics of AP and CT when S2 was delivered with a 10-ms coupling interval (Fig. 2C). Although detailed simulations are required to elucidate accurately the mechanism of CT delay, examining the current-voltage relationships for I_{CaL} and NCX current ($I_{Na/Ca}$) would be a reasonable way to estimate the approximate contributions of these two main Ca^{2+} currents in the effect of V_m – Ca dissociation. In diastole, $I_{Na/Ca}$ has a reversal potential between −20 and −40 mV [6,41] and becomes more positive during the AP [67]. At the beginning of the AP, when V_m exceeds the NCX equilibrium potential, $I_{Na/Ca}$ changes direction and brings Ca^{2+} into the cell. The strong stimulus during depolarization phase of the AP increases upstroke velocity and AP amplitude at the VC region and thereby facilitates NCX-mediated entry of Ca^{2+}. The current-voltage relationship for I_{CaL} in rabbit cardiomyocytes has a minimum near 10 mV and a reversal potential of about 60 mV [32,47]. The quick and strong depolarization due to rapidly approaching the reversal potential will reduce the driving force for Ca^{2+} entry and hence lessen I_{CaL}. Because I_{CaL} is primarily responsible for activation of ryanodine receptors, the net result is observed in delayed CT dynamics. While the V_m – Ca dissociation was observed under normal conditions during steady pacing, it may play a role in defibrillation outcome by means of APD alteration. It could also be involved in the shock-induced heterogeneous distribution of Ca^{2+}. Recently Hwang *et al.* found that the first activation during unsuccessful defibrillation associates with a region of low $[Ca^{2+}]_i$ surrounded by elevated $[Ca^{2+}]_i$ ("Ca^{2+} sinkholes") [30]. The shock-mediated delay of CT upstroke at areas with lower V_m could be responsible for the occurrence of "Ca^{2+} sinkholes".

The VC-associated lengthening of CT, which becomes more prominent for coupling intervals longer than 50 ms, occurs by elevation of $[Ca^{2+}]_i$ due to VC positive polarization (Fig. 2C and Fig. 3C). The CT prolongation at VA areas is caused by elevation of V_m after S2 termination (Fig. 2D and Fig. 3D). Analysis of stimulation in the refractory period and in resting tissue revealed that $[Ca^{2+}]_i$, similar to V_m, exhibits four basic stimulation modes: cathodal and anodal make, and cathodal and anodal break stimulation. Furthermore, break stimulation can be followed by reentry (Fig. 5B). Similar results were reported by Sidorov *et al.*, [55] and recently observed by Gray *et al.* [26], where V_m and Ca^{2+} state-space dynamics were studied during quatrefoil reentry initiation. Stimulation in resting tissue exhibited VA and VC-related delays in CT upstroke resulting in four-petalled $d[Ca^{2+}]_i/dt$ patterns that were observed under both cathodal and anodal stimulation (Fig. 5C and 6C).

Many optical imaging studies minimize motion artifacts by the use of one of a variety of contraction blocking agents. Of these, BDM is cost-effective, widely accepted, and was chosen when this study was designed and implemented. Only recently has a novel selective excitation-contraction uncoupler, blebbistatin [1,59], been applied to cardiac imaging [16,21]. Because BDM exhibits a phosphatase-like activity [14,29] and has additional side effects on the SR [58], Ca^{2+} channel currents [39] and AP characteristics [34], we conducted a series of experiments with blebbistatin, which acts by inhibiting myosin II isoforms and does not affect intracellular CT. The results were qualitatively similar to those obtained in experiments using BDM. Specifically, the VC and VA-associated changes in $[Ca^{2+}]_i$ during the early AP plateau phase for coupling intervals between 30 and 70 ms in Figure 5A correlate with those illustrated in Figures 2B and 3B. However, some differences do exist in the behavior of $[Ca^{2+}]_i$ as a function of S1-S2 interval between experiments with BDM (Fig. 4B) and blebbistatin (Fig. 5B). The $\Delta[Ca^{2+}]_i$ curves are more horizontal when blebbistatin was utilized (Fig. 5B) than under BDM (Fig. 4B). In particular, the anodal curve intersects the zero line at coupling interval of 175 ms (Fig. 5B), whereas this value is 155 ms when BDM was applied (Fig. 4B). This discrepancy is a result of AP shortening due to BDM [10,40] and slight prolongation of AP duration caused by blebbistatin [21].

In summary, our results demonstrate the variety of spatial and temporal responses of two variables (V_m and $[Ca^{2+}]_i$) induced on the surface of the whole heart by unipolar stimuli as a function of polarity and coupling interval. For the majority of coupling intervals the Ca^{2+} response was directly related to the V_m response after a short delay, as occurs during normal heart function. However, at very short coupling intervals the V_m and $[Ca^{2+}]_i$ responses were not positively correlated. This fact has implications, especially for defibrillation because any differences in V_m and $[Ca^{2+}]_i$ responses are likely to be important (*e.g.*, either proarrhythmic or antiarrhythmic). This in turn suggests that V_m and $[Ca^{2+}]_i$ are well-suited as orthogonal variables for recording phase plane trajectories during shocks and reentry [26]. In addition, the quality and detail of our data and the range of parameters over which it was collected offer an opportunity for quantitative tests of the accuracy and ability of numerical models of cardiac tissue to fully reproduce and explain the spatiotemporal relationships between V_m and Ca^{2+} signals during point stimulation [2], AP propagation, and calcium transport in the cardiac bidomain.

Acknowledgments

This work was supported by the NIH (RO1-HL58241, RO1-HL63267), the American Heart Association (0635037N), and the Vanderbilt Institute for Integrative Biosystems Research and Education. We thank Allison Price and Don Berry for their editorial assistance.

Abbreviations

$[Ca^{2+}]_i$, intracellular calcium concentration
V_m, transmembrane potential
AP, action potential
CT, calcium transient
S1, conditioning stimulus
S2, testing stimulus
SR, sarcoplasmic reticulum
VT, ventricular tachycardia
VF, ventricular fibrillation
VC, virtual cathode
VA, virtual anode
NCX, Na^+/Ca^{2+} exchanger

I_{CaL}, current via the L-type Ca^{2+} channels
$I_{Na/Ca}$, current via Na^{+}/Ca^{2+} exchanger

References

1. Allingham JS, Smith R, Rayment I. The structural basis of blebbistatin inhibition and specificity for myosin II. Nat Struct Mol Biol 2005;12:378–379. [PubMed: 15750603]
2. Ashihara T, Trayanova NA. Asymmetry in membrane responses to electric shocks: insights from bidomain simulations. Biophys J 2004;87:2271–2282. [PubMed: 15454429]
3. Baxter WT, Mironov SF, Zaitsev AV, Jalife J, Pertsov AM. Visualizing excitation waves inside cardiac muscle using transillumination. Biophys J 2001;80:516–530. [PubMed: 11159422]
4. Bers DM. Ca transport during contraction and relaxation in mammalian ventricular muscle. Basic Res Cardiol 1997;92(Suppl 1):1–10. [PubMed: 9202838]
5. Bers, DM. Excitation-contraction coupling and cardiac contractile force. Kluwer Academic; Dordrecht: 2001.
6. Bers DM, Barry WH, Despa S. Intracellular Na+ regulation in cardiac myocytes. Cardiovasc Res 2003;57:897–912. [PubMed: 12650868]
7. Bray MA, Wikswo JP. Examination of optical depth effects on fluorescence imaging of cardiac propagation. Biophys J 2003;85:4134–4145. [PubMed: 14645100]
8. Cheek ER, Fast VG. Nonlinear changes of transmembrane potential during electrical shocks: role of membrane electroporation. Circ Res 2004;94:208–214. [PubMed: 14670844]
9. Cheng DK, Tung L, Sobie EA. Nonuniform responses of transmembrane potential during electric field stimulation of single cardiac cells. Am J Physiol 1999;277:H351–H362. [PubMed: 10409215]
10. Cheng Y, Li L, Nikolski V, Wallick DW, Efimov IR. Shock-induced arrhythmogenesis is enhanced by 2,3-butanedione monoxime compared with cytochalasin D. Am J Physiol Heart Circ Physiol 2004;286:H310–H318. [PubMed: 12958029]
11. Choi BR, Salama G. Simultaneous maps of optical action potentials and calcium transients in guinea-pig hearts: mechanisms underlying concordant alternans. J Physiol (Lond) 2000;529:171–188. [PubMed: 11080260]
12. Chudin E, Goldhaber J, Garfinkel A, Weiss J, Kogan B. Intracellular Ca(2+) dynamics and the stability of ventricular tachycardia. Biophys J 1999;77:2930–2941. [PubMed: 10585917]
13. Cohen NM, Lederer WJ. Changes in the calcium current of rat heart ventricular myocytes during development. J Physiol 1988;406:115–146. [PubMed: 2855434]
14. Davies DR, Green AL. The kinetics of reactivation, by oximes, of cholinesterase inhibited by organophosphorus compounds. Biochem J 1956;63:529–535. [PubMed: 13355845]
15. Ding L, Splinter R, Knisley SB. Quantifying spatial localization of optical mapping using Monte Carlo simulations. IEEE Trans Biomed Eng 2001;48:1098–1107. [PubMed: 11585033]
16. Dou Y, Arlock P, Arner A. Blebbistatin specifically inhibits actin-myosin interaction in mouse cardiac muscle. Am J Physiol Cell Physiol 2007;293:C1148–C1153. [PubMed: 17615158]
17. Efimov IR, Sidorov V, Cheng Y, Wollenzier B. Evidence of three-dimensional scroll waves with ribbon-shaped filament as a mechanism of ventricular tachycardia in the isolated rabbit heart. J Cardiovasc Electrophysiol 1999;10:1452–1462. [PubMed: 10571365]
18. Escobar AL, Ribeiro-Costa R, Villalba-Galea C, Zoghbi ME, Perez CG, Mejia-Alvarez R. Developmental changes of intracellular Ca2+ transients in beating rat hearts. Am J Physiol Heart Circ Physiol 2004;286:H971–H978. [PubMed: 14644760]
19. Fast VG, Rohr S, Ideker RE. Nonlinear changes of transmembrane potential caused by defibrillation shocks in strands of cultured myocytes. Am J Physiol Heart Circ Physiol 2000;278:H688–H697. [PubMed: 10710335]
20. Fast VG, Cheek ER, Pollard AE, Ideker RE. Effects of electrical shocks on Cai2+ and Vm in myocyte cultures. Circ Res 2004;94:1589–1597. [PubMed: 15155528]
21. Fedorov VV, Lozinsky IT, Sosunov EA, Anyukhovsky EP, Rosen MR, Balke CW, Efimov IR. Application of blebbistatin as an excitation-contraction uncoupler for electrophysiologic study of rat and rabbit hearts. Heart Rhythm 2007;4:619–626. [PubMed: 17467631]

22. Girouard SD, Laurita KR, Rosenbaum DS. Unique properties of cardiac action potentials recorded with voltage-sensitive dyes. J Cardiovasc Electrophysiol 1996;7:1024–1038. [PubMed: 8930734]
23. Gomez JP, Potreau D, Branka JE, Raymond G. Developmental changes in Ca2+ currents from newborn rat cardiomyocytes in primary culture. Pflugers Arch 1994;428:241–249. [PubMed: 7816546]
24. Gray RA. What exactly are optically recorded “action potentials”? J Cardiovasc Electrophysiol 1999;10:1463–1466. [PubMed: 10571366]
25. Gray RA, Huelsing DJ, Aguel F, Trayanova NA. Effect of strength and timing of transmembrane current pulses on isolated ventricular myocytes. J Cardiovasc Electrophysiol 2001;12:1129–1137. [PubMed: 11699521]
26. Gray RA, Iyer A, Bray MA, Wikswo JP. Voltage-calcium state-space dynamics during initiation of reentry. Heart Rhythm 2006;3:247–248. [PubMed: 16443544]
27. Guo W, Kamiya K, Cheng J, Toyama J. Changes in action potentials and ion currents in long-term cultured neonatal rat ventricular cells. Am J Physiol 1996;271:C93–102. [PubMed: 8760034]
28. Holcomb MR, Woods MC, Uzelac I, Wikswo JP, Gilligan JM, Sidorov VY. Dual camera system for multimodal imaging of cardiac electrophysiology and metabolism. 2008Submitted
29. Holmstedt B. Pharmacology of organophosphorus cholinesterase inhibitors. Pharmacol Rev 1959;11:567–688. [PubMed: 14402820]
30. Hwang GS, Hayashi H, Tang L, Ogawa M, Hernandez H, Tan AY, Li H, Karagueuzian HS, Weiss JN, Lin SF, Chen PS. Intracellular calcium and vulnerability to fibrillation and defibrillation in Langendorff-perfused rabbit ventricles. Circulation 2006;114:2595–2603. [PubMed: 17116770]
31. Janks DL, Roth BJ. Averaging over depth during optical mapping of unipolar stimulation. IEEE Trans Biomed Eng 2002;49:1051–1054. [PubMed: 12214878]
32. Josephson IR, Sanchez-Chapula J, Brown AM. A comparison of calcium currents in rat and guinea pig single ventricular cells. Circ Res 1984;54:144–156. [PubMed: 6319043]
33. Katz, AM. Excitation-contraction coupling: calcium fluxes across the sarcoplasmic reticulum. In: Katz, AM., editor. Physiology of the heart. Lippincott Williams & Wilkins; Philadelphia: 2001. p. 216-239.
34. Kettlewell S, Walker NL, Cobbe SM, Burton FL, Smith GL. The electrophysiological and mechanical effects of 2,3-butane-dione monoxime and cytochalasin-D in the Langendorff perfused rabbit heart. Exp Physiol 2004;89:163–172. [PubMed: 15123545]
35. Keung EC, Keung CS, Aronson RS. Passive electrical properties of normal and hypertrophied rat myocardium. Am J Physiol 1982;243:H917–H926. [PubMed: 6216816]
36. Kleber AG, Riegger CB. Electrical constants of arterially perfused rabbit papillary muscle. J Physiol 1987;385:307–324. [PubMed: 3656162]
37. Knisley SB. Transmembrane voltage changes during unipolar stimulation of rabbit ventricle. Circ Res 1995;77:1229–1239. [PubMed: 7586236]
38. Kukushkin NI, Bukauskas FF, Sakson ME, Nasonova VV. [Anisotropy of stationary rates and delays in extrasystolic waves in the dog heart]. Biofizika 1975;20:687–692. [PubMed: 1201305]
39. Lang RJ, Paul RJ. Effects of 2,3-butanedione monoxime on whole-cell Ca2+ channel currents in single cells of the guinea-pig taenia caeci. J Physiol 1991;433:1–24. [PubMed: 1726794]
40. Lee MH, Lin SF, Ohara T, Omichi C, Okuyama Y, Chudin E, Garfinkel A, Weiss JN, Karagueuzian HS, Chen PS. Effects of diacetyl monoxime and cytochalasin D on ventricular fibrillation in swine right ventricles. Am J Physiol Heart Circ Physiol 2001;280:H2689–H2696. [PubMed: 11356625]
41. Litwin SE, Li J, Bridge JH. Na-Ca exchange and the trigger for sarcoplasmic reticulum Ca release: studies in adult rabbit ventricular myocytes. Biophys J 1998;75:359–371. [PubMed: 9649393]
42. Maack C, O'Rourke B. Excitation-contraction coupling and mitochondrial energetics. Basic Res Cardiol 2007;102:369–392. [PubMed: 17657400]
43. Neunlist M, Tung L. Spatial distribution of cardiac transmembrane potentials around an extracellular electrode: dependence on fiber orientation. Biophys J 1995;68:2310–2322. [PubMed: 7647235]
44. Nuss HB, Marban E. Electrophysiological properties of neonatal mouse cardiac myocytes in primary culture. J Physiol 1994;479(Pt 2):265–279. [PubMed: 7799226]

45. Olivetti G, Anversa P, Loud AV. Morphometric study of early postnatal development in the left and right ventricular myocardium of the rat. II. Tissue composition, capillary growth, and sarcoplasmic alterations. Circ Res 1980;46:503–512. [PubMed: 6444555]
46. Omichi C, Lamp ST, Lin SF, Yang J, Baher A, Zhou S, Attin M, Lee MH, Karagueuzian HS, Kogan B, Qu Z, Garfinkel A, Chen PS, Weiss JN. Intracellular Ca dynamics in ventricular fibrillation. Am J Physiol Heart Circ Physiol 2004;286:H1836–H1844. [PubMed: 14704235]
47. Puglisi JL, Yuan W, Bassani JWM, Bers DM. Ca2+ influx through Ca2+ channels in rabbit ventricular myocytes during action potential clamp: Influence of temperature. Circ Res 1999;85:7e–16.
48. Raman V, Pollard AE, Fast VG. Shock-induced changes of Ca(i)2+ and Vm in myocyte cultures and computer model: Dependence on the timing of shock application. Cardiovasc Res 2007;73:101–110. [PubMed: 17134687]
49. Ruiz-Meana M, Abellan A, Miro-Casas E, Garcia-Dorado D. Opening of mitochondrial permeability transition pore induces hypercontracture in Ca(2+) overloaded cardiac myocytes. Basic Res Cardiol 2007;102:542–552. [PubMed: 17891523]
50. Sato D, Shiferaw Y, Garfinkel A, Weiss JN, Qu Z, Karma A. Spatially discordant alternans in cardiac tissue: role of calcium cycling. Circ Res 2006;99:520–527. [PubMed: 16902177]
51. Schlotthauer K, Bers DM. Sarcoplasmic reticulum Ca(2+) release causes myocyte depolarization. Underlying mechanism and threshold for triggered action potentials. Circ Res 2000;87:774–780. [PubMed: 11055981]
52. Sepulveda NG, Roth BJ, Wikswo JP Jr. Current injection into a two-dimensional anisotropic bidomain. Biophys J 1989;55:987–999. [PubMed: 2720084]
53. Sepulveda NG, Wikswo JP Jr. Electric and magnetic fields from two-dimensional anisotropic bisyncytia. Biophys J 1987;51:557–568. [PubMed: 3580484]
54. Sharma V, Tung L. Effects of uniform electric fields on intracellular calcium transients in single cardiac cells. Am J Physiol Heart Circ Physiol 2002;282:H72–H79. [PubMed: 11748049]
55. Sidorov VY, Woods MC, Holcomb MR, Wikswo JP. Optical mapping of calcium distribution reveals make and break excitation modes. Heart Rhythm 2005;2:S216.
56. Sidorov VY, Woods MC, Wikswo JP. Effects of elevated extracellular potassium on the stimulation mechanism of diastolic cardiac tissue. Biophys J 2003;84:3470–3479. [PubMed: 12719272]
57. Snopko RM, Aromolaran AS, Karko KL, Ramos-Franco J, Blatter LA, Mejia-Alvarez R. Cell culture modifies Ca2+ signaling during excitation-contraction coupling in neonate cardiac myocytes. Cell Calcium 2007;41:13–25. [PubMed: 16908061]
58. Steele DS, Smith GL. Effects of 2,3-butanedione monoxime on sarcoplasmic reticulum of saponin-treated rat cardiac muscle. Am J Physiol 1993;265:H1493–H1500. [PubMed: 8238560]
59. Straight AF, Cheung A, Limouze J, Chen I, Westwood NJ, Sellers JR, Mitchison TJ. Dissecting temporal and spatial control of cytokinesis with a myosin II inhibitor. Science 2003;299:1743–1747. [PubMed: 12637748]
60. Studer R, Reinecke H, Vetter R, Holtz J, Drexler H. Expression and function of the cardiac Na+/Ca2+ exchanger in postnatal development of the rat, in experimental-induced cardiac hypertrophy and in the failing human heart. Basic Res Cardiol 1997;92(Suppl 1):53–58. [PubMed: 9202844]
61. ter Keurs HE, Wakayama Y, Sugai Y, Price G, Kagaya Y, Boyden PA, Miura M, Stuyvers BD. Role of sarcomere mechanics and Ca2+ overload in Ca2+ waves and arrhythmias in rat cardiac muscle. Ann N Y Acad Sci 2006;1080:248–267. [PubMed: 17132788]
62. Tibbits GF, Xu L, Sedarat F. Ontogeny of excitation-contraction coupling in the mammalian heart. Comp Biochem Physiol A Mol Integr Physiol 2002;132:691–698. [PubMed: 12095856]
63. Wahler GM, Dollinger SJ, Smith JM, Flemal KL. Time course of postnatal changes in rat heart action potential and in transient outward current is different. Am J Physiol 1994;267:H1157–H1166. [PubMed: 8092281]
64. Warren M, Huizar JF, Shvedko AG, Zaitsev AV. Spatiotemporal relationship between intracellular Ca2+ dynamics and wave fragmentation during ventricular fibrillation in isolated blood-perfused pig hearts. Circ Res 2007;101:e90–101. [PubMed: 17932324]
65. Wibo M, Bravo G, Godfraind T. Postnatal maturation of excitation-contraction coupling in rat ventricle in relation to the subcellular localization and surface density of 1,4-dihydropyridine and ryanodine receptors. Circ Res 1991;68:662–673. [PubMed: 1660357]

66. Wikswo JP Jr. Lin SF, Abbas RA. Virtual electrodes in cardiac tissue: a common mechanism for anodal and cathodal stimulation. Biophys J 1995;69:2195–2210. [PubMed: 8599628]

67. Wu S, Weiss JN, Chou C-C, Attin M, Hayashi H, Lin S-F. Dissociation of membrane potential and intracellular calcium during ventricular fibrillation. J Cardiovasc Electrophysiol 2005;16:186–192. [PubMed: 15720458]

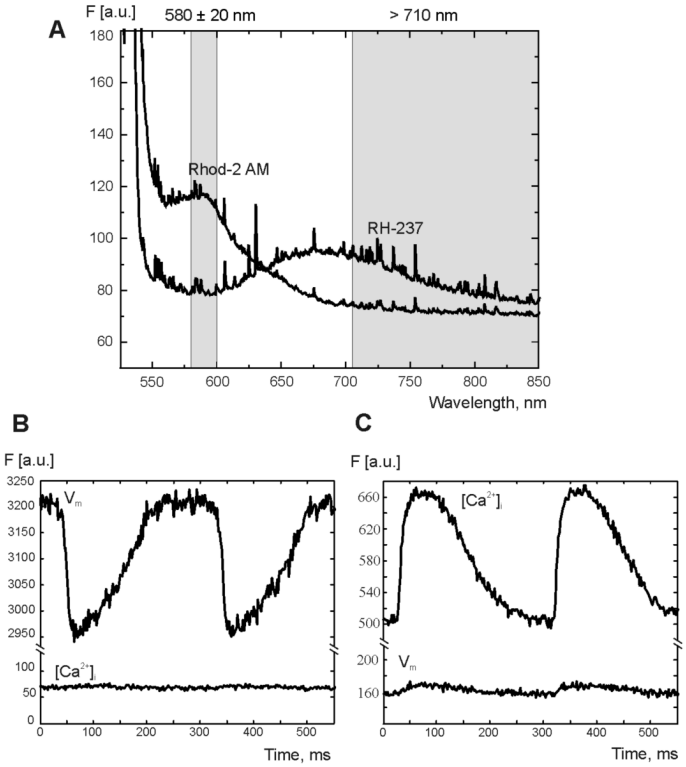

Figure 1. Rhod-2AM and RH-237 fluorescence measured in the heart

(A) Emission spectra of Rhod-2AM and RH-237. The two vertical gray bands illustrate the light transmission for the band pass (580 ± 20 nm) and long pass (> 710 nm) filters. (B and C) Changes in fluorescence recorded at one pixel when the heart was only stained with either RH-237 (B) or Rhod-2 AM (C) alone.

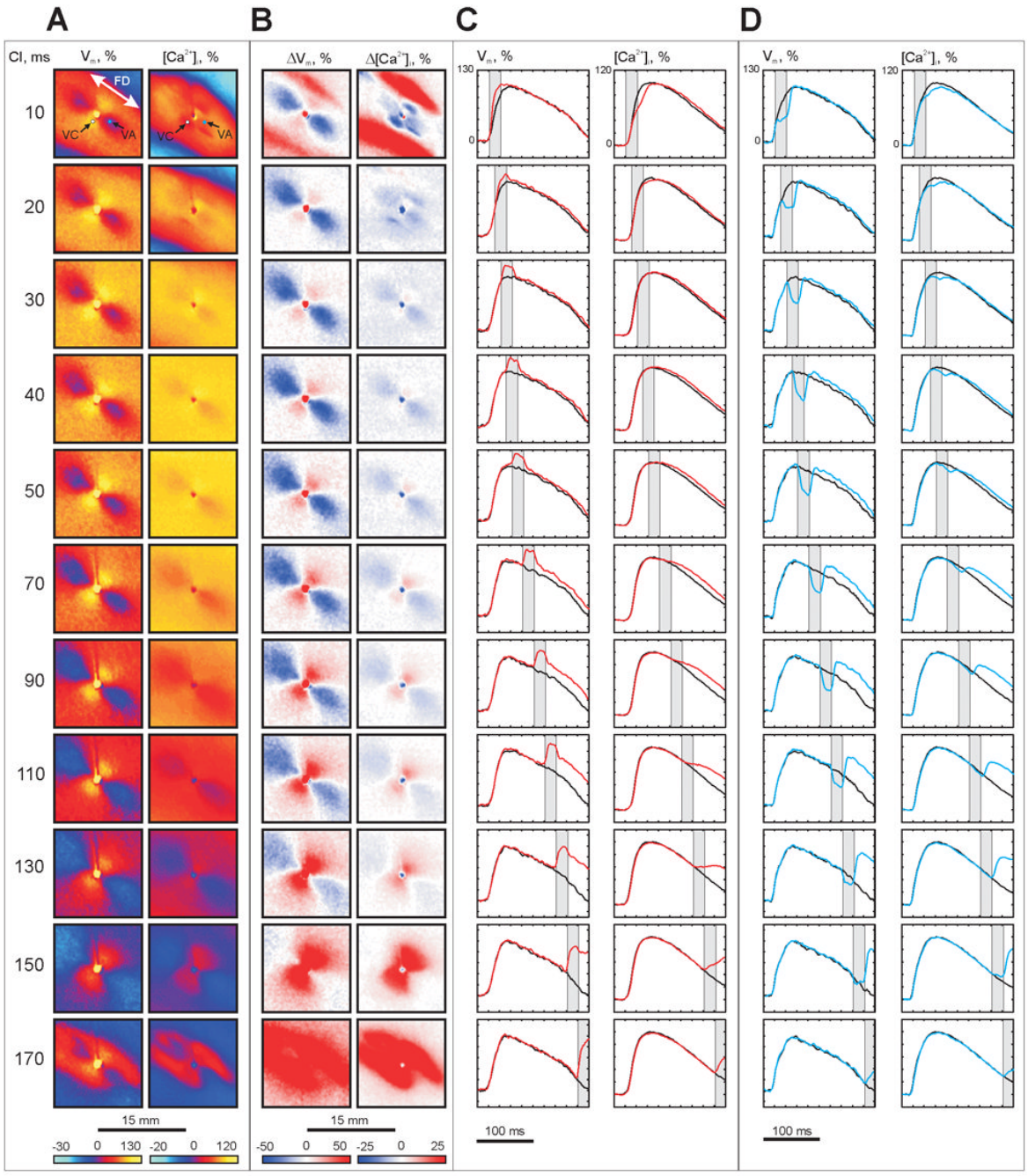

Figure 2. V_m and $[Ca^{2+}]_i$ changes induced by S2 (−20 mA, 20 ms) as a function of S1-S2 interval

(A) V_m and $[Ca^{2+}]_i$ distributions at the end of S2. (B) ΔV_m and $\Delta [Ca^{2+}]_i$ distributions at the end of S2. (C) Action potentials (APs) and calcium transients (CTs) within the virtual cathode (white dot in A) resulting from S1-S2 stimulation (red trace) are superimposed on the signals obtained from the same pixel when S1 alone was used (black trace). (D) APs and CTs (blue) within the virtual anode (blue dot in A) are superimposed on the traces resulting from S1 (black). The vertical gray bands indicate S2 timing. The numbers on the far left are S1-S2 intervals in ms. The image size in A and B is 15 × 15 mm^2.

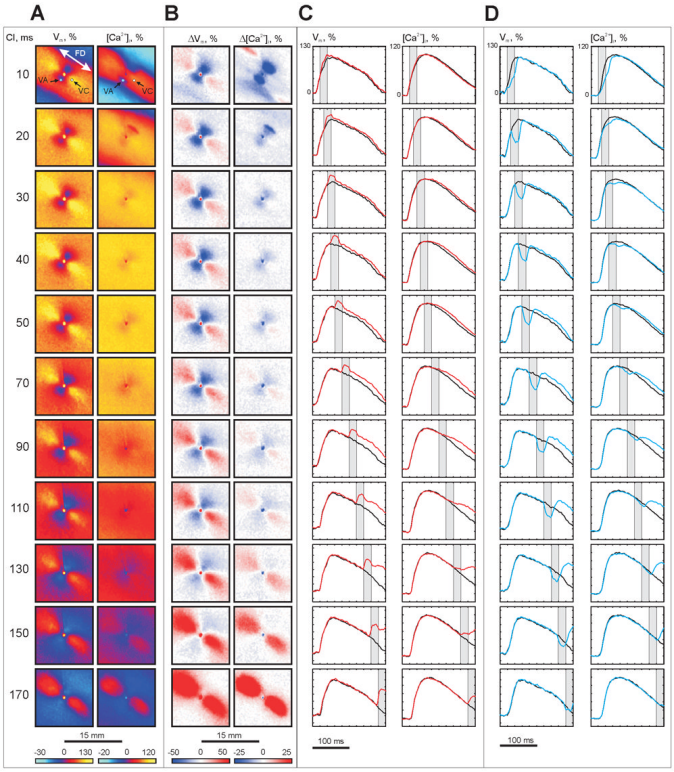

Figure 3. V_m and $[Ca^{2+}]_i$ changes induced by S2 (+20 mA, 20 ms) as a function of S1-S2 interval

(A) V_m and $[Ca^{2+}]_i$ distributions at the end of S2. (B) ΔV_m and $\Delta[Ca^{2+}]_i$ distributions at the end of S2. (C) S1-S2 VC traces (red) are superimposed on the signals induced with S1 alone (black). (D) S1-S2 VA traces (blue) are superimposed on the signals induced with S1 alone (black). The pixel locations of the traces are indicated by white and blue dots in A.

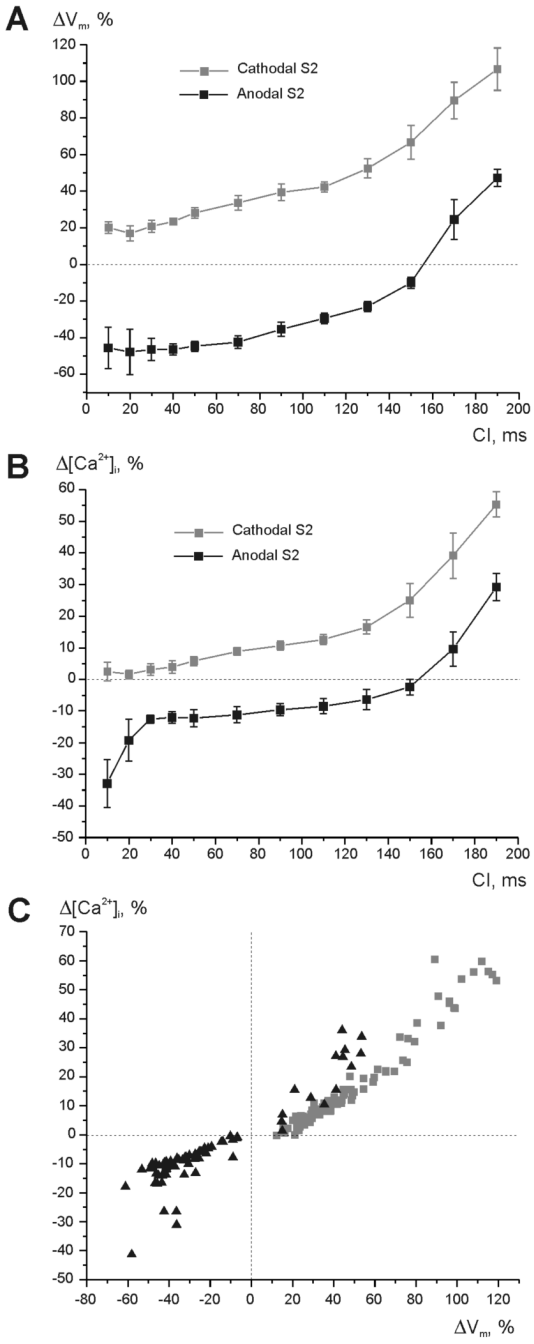

Figure 4. The maximum V_m and $[Ca^{2+}]_i$ alterations at the central virtual electrode region during the shock as a function of S1-S2 interval

(A) V_m changes during cathodal (grey) and anodal (black) stimulation. (B) $[Ca^{2+}]_i$ changes during cathodal (gray) and anodal (black) shocks. (C) $\Delta[Ca^{2+}]_i$ versus ΔV_m for cathodal stimulation (gray squares) and anodal stimulation (black triangles) for all acquired data. S1-S2 interval ranges from 10 to 190 ms. The area directly beneath the electrode was excluded from analysis to avoid artifacts due to electroporation. Seven experiments were analyzed.

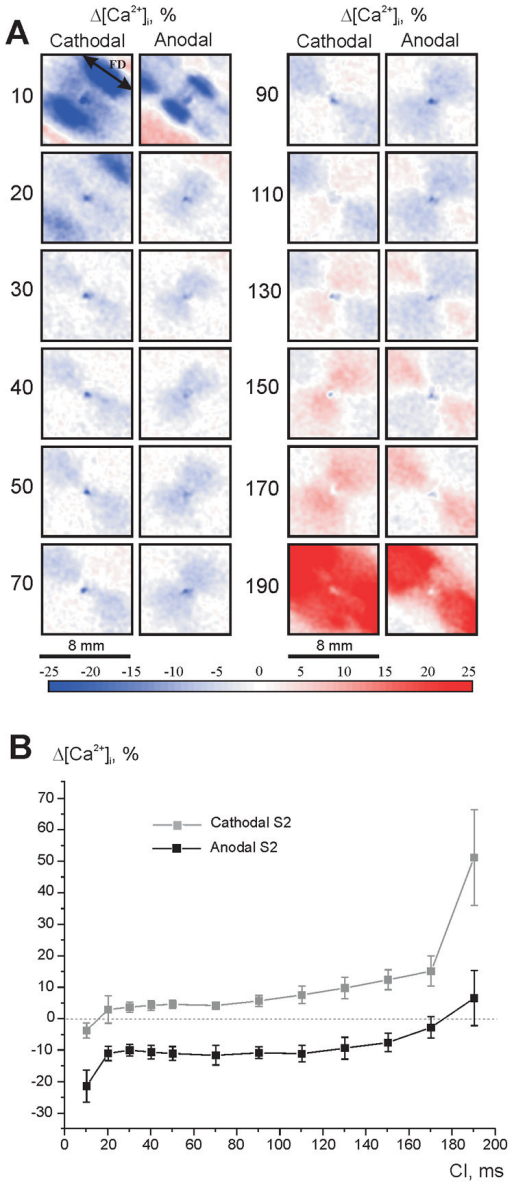

Figure 5. $[Ca^{2+}]_i$ changes induced by cathodal and anodal S2 (20 mA, 20 ms) as a function of S1-S2 interval using blebbistatin as the uncoupler

(A) $\Delta[Ca^{2+}]_i$ distribution at the end of S2. The image size is 8 × 8 mm^2. The numbers show coupling interval in ms. (B) The maximum $[Ca^{2+}]_i$ alterations in the central virtual electrode region during the shock.

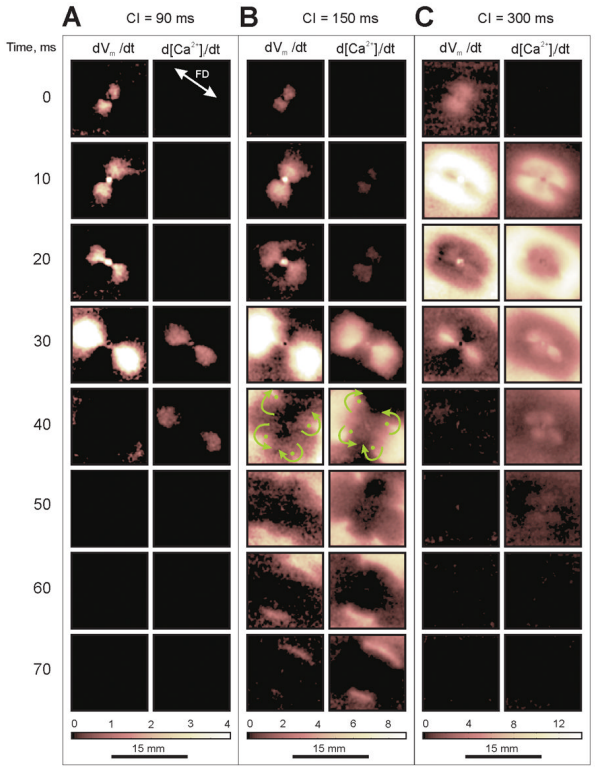

Figure 6. V_m and $[Ca^{2+}]_i$ outcomes from cathodal stimulation

False color images represent V_m and $[Ca^{2+}]_i$ derivatives as a function of time since S2 onset. The black color indicates no change in V_m and $[Ca^{2+}]_i$, and the white color corresponds to the maximum change in V_m and $[Ca^{2+}]_i$. (A) Non-propagating response at an S1-S2 interval of 90 ms. (B) Break stimulation at an S1-S2 interval of 150 ms. (C) Make stimulation at an S1-S2 interval of 300 ms. Green arrows in panel B indicate the direction of wave front propagation around the green dots.

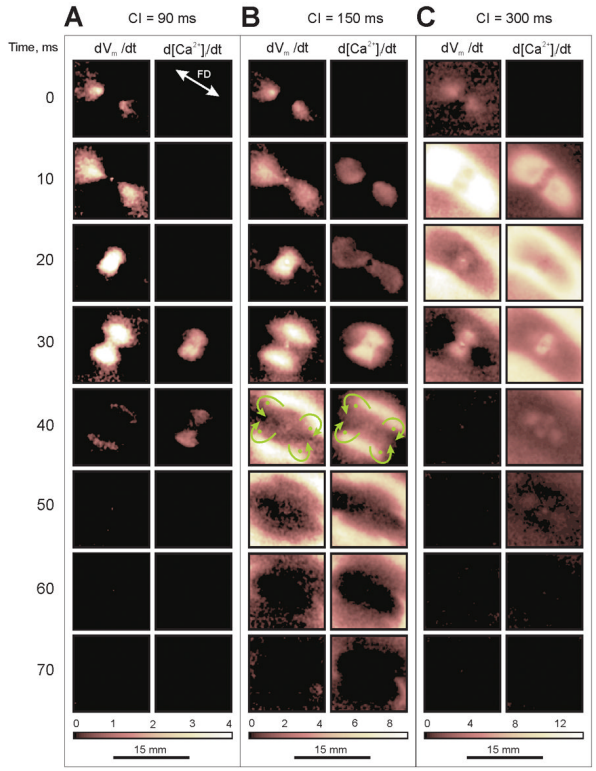

Figure 7. V_m and $[Ca^{2+}]_i$ outcomes from anodal stimulation

The S1-S2 intervals for (A) non-propagating response, (B) break stimulation and (C) make stimulation are the same as in Figure 6. Green arrows in panel B indicate the direction of wave front propagation around the green dots.